Accurate 3D Thermal Network Development for Direct-drive Outer-rotor Hybrid-PM Flux-switching Generator

Ali Zarghani[1], *Mohammad Farahzadi*[2], *Aghil Ghaheri*[1*] *and Karim Abbaszadeh*[3]

(1. Faculty of Electrical Engineering, Shahid Beheshti University, Tehran 1983969411, Iran;
2. Faculty of Electrical Engineering, University of Science and Culture, Tehran 1461968151, Iran;
3. Department of Electrical Engineering, K. N. Toosi University of Technology, Tehran 1631714191, Iran)

Abstract: Heat and thermal problems are major obstacles to achieving high power density in compact permanent magnet (PM) topologies. Consequently, a comprehensive, accurate, and rapid temperature rise estimation method is required for novel electric machines to ensure safe and reliable operations. A unique three-dimensional (3D) lumped parameter thermal network (LPTN) is presented for accurate thermal modeling of a newly developed outer-rotor hybrid-PM flux switching generator (OR-HPMFSG) for direct-drive applications. First, the losses of the OR-HPMFSG are calculated using 3D finite element analysis (FEA). Subsequently, all machine components considering the thermal contact resistance, anisotropic thermal conductivity of materials, and various heat flow paths are comprehensively modeled based on the thermal resistances. In the proposed 3-D LPTN, internal nodes are considered to predict the average temperature as well as the hot spots of all active and passive components. Experimental measurements are performed on a prototype OR-HPMFSG to validate the efficiency of the 3-D LPTN. A comparison of the results at various operating points between the developed 3-D LPTN, experimental test, and FEA indicates that the 3-D LPTN quickly approximates the hotspot and mean temperature of all components under both transient and steady states with high accuracy.

Keywords: Direct-drive wind turbine, hybrid-PM flux switching generator, lumped parameter thermal network, temperature estimation, 3D thermal modeling

1 Introduction

Direct-drive wind turbines (DDWTs) are favorable at low-power levels owing to their high energy yield, compact design (owing to the lack of a mechanical device), easy assembly, less acoustic noise, and remarkable efficiency [1].

Since permanent-magnet (PM) generators have a high power density, they are well suited for low-power DDWT applications. Among the PM topologies [2], there has been an uptick in the utilization of compact flux-switching PM (FSPM) machines in industrial applications, particularly in DDWTs, primarily owing to their outstanding magnetic advantages [3]. However, completely enclosed FSPMs have considerable loss density and temperature rise problems due to their compact construction, concentration of major loss sources, and poor heat dissipation from the PM sandwiched between the stator poles. The temperature rise diminishes the power density by changing the operating point of the PM or by demagnetization [4]. Similarly, exceeding the critical temperature causes winding insulation failure [5-6]. Additionally, complex changes in materials and fatigue damage further aggravate the effects of high temperatures from a mechanical aspect [7]. These factors limit the lifespan and reliability of the FSPMs for DDWTs. Therefore, the thermal analysis of FSPMs is of utmost significance.

For the thermal modeling of electrical machines, analytical and numerical approaches are often utilized. Numerical methods such as finite element analysis (FEA) and computational fluid dynamics (CFD) are widely used to extract precise temperature distributions [8] and evaluate the cooling

Manuscript received October 9, 2023; revised November 30, 2023; accepted January 15, 2024. Date of publication June 30, 2024; date of current version May 8, 2024.

* Corresponding Author, E-mail: a_ghaheri@sbu.ac.ir

Digital Object Identifier: 10.23919/CJEE.2024.000059

performance [9]. FEA and CFD are powerful tools for analyzing complex three-dimensional (3D) geometries, obtaining temperature distributions, and estimating heat-flow paths. However, a substantial amount of time and resource intensive systems are required to solve iterative matrices [10]. The analytical approach of the lumped parameter thermal network (LPTN), rapidly determines the temperature of components while maintaining an acceptable level of accuracy and incurring the least possible computing expense. Recently, the LPTN approach has gained increasing attention as an innovative PM topology for predicting the maximum temperature in the PM [11] and winding [12]. Both dynamic [13] and static [14] LPTNs have been developed for conventional FSPMs. Moreover, Ref. [15] investigated the effectiveness of a water-cooling system using a three-dimensional (3-D) LPTN. The problem of high temperature in the internal winding owing to poor heat dissipation in double-rotor FSPM topologies was studied using LPTN in Refs. [16-17]. Contrary to Refs. [13-17], where LPTNs are performed for FSPMs whose excitation is on the stator, Ref. [18] designed a 3-D LPTN specific to rotor-excited axial-field FSPM. In Refs. [13-18], the average temperature of the components was derived. Evidently, designing a LPTN is highly dependent on the machine configuration because internal fluid dynamics and flux paths vary for different topologies.

Although previous studies have proposed LPTNs for different FSPMs whose excitation was on the stator or rotor, there is a lack of contribution on the outer-rotor hybrid PM flux-switching generator (OR-HPMFSG) with PMs located in both the stator and rotor. To fill this gap, this study aims to develop a unique 3-D LPTN for the OR-HPMFSG, where NdFeB PMs are sandwiched between the outer rotor segments and ferrite PMs are inserted into the stator yoke. A detailed and accurate 3-D LPTN, which has the potential to be used in the design algorithms of OR-HPMFSGs with various power levels and operating conditions, is proposed to predict the maximum and average temperatures of all components in both the transient and steady states. The remainder of this paper is organized as follows. The new structure of the prototype OR-HPMFSG and its loss assessment are discussed in Section 2. In Section 3, the heat transfer paths are extracted, and each component of the OR-HPMFSG is modeled using thermal resistances and capacitances to design a unique 3-D LPTN. Finally, in Section 4, the results of the proposed 3-D LPTN are compared with those of an experimental test and 3-D FEA at various operating points to validate its high accuracy and calculation speed.

2 Study on the prototyped OR-HPMFSG

In this section, the structure and concept of the OR-HPMFSG as well as the losses, which are thermal characteristics, are investigated.

The OR-HPMFSG is equipped with two types of PMs, which are sandwiched and located in the outer rotor segments and stator yoke, respectively. Consequently, the higher power density and lower PM volume are the distinct advantages of the OR-HPMFSG compared with conventional FSPMs [19]. The components of the manufactured generator are shown in Fig. 1. The stator laminations composed of silicon steel M600 are affixed to a stationary shaft made of structural steel 316. The fixed components of the prototype generator were formed by adding windings and AC-8 grade ferrite PMs. Each N35 grade NdFeB PM is sandwiched between two rotor segments, after which they are stuck to the aluminum holder. The rotating components were completed by attaching a rotating shaft and two end caps. Finally, the fixed components, rotating components, and iron pillars were assembled. The specifications of the 24/10, 125 Hz, and 2.3 kW OR-HPMFSG, designed for DDWT applications, are listed in Tab. 1.

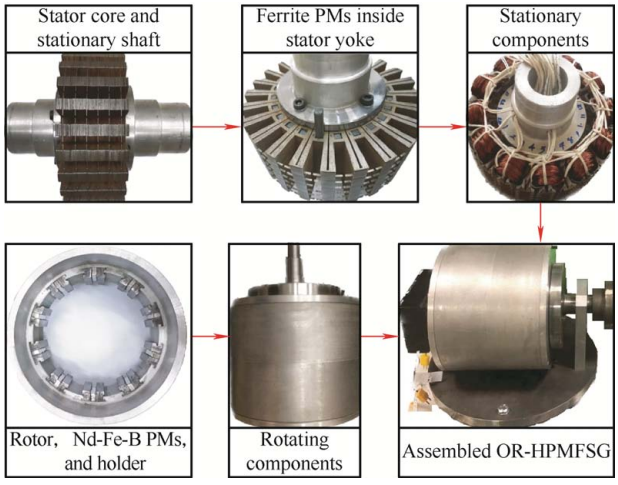

Fig. 1 Prototyped OR-HPMFSG

Tab. 1 Rated specification of OR-HPMFSG

Parameter	Value
Output power/kW	2.3
Air-gap length/mm	0.65
Active length/mm	60
Rotor outer diameter/mm	200.7
Stator outer diameter/mm	170
Stator pole number	24
Rotor pole number	10
Rotational speed/(r/min)	750
Residual flux density of neodymium PM/T	1.2
Residual flux density of ferrite PM/T	0.41

In this configuration, the magnetization directions of the stator and rotor PMs are arranged such that they increase the magneto-motive force that is produced at one pole. As shown in Fig. 2a, the magnetization directions of the rotor and stator PMs are counterclockwise and clockwise, respectively, leading to an increase in the magnetomotive force at one pole. Importantly, the created flux barrier inside the stator teeth not only separates the positive and negative half cycles of the flux linkage that exists between the rotor segments and stator teeth, but also helps decrease the risk of winding insulator failure. The magnetic flux density extracted by 3-D FEA, is shown in Fig. 2b. Saturation did not occur in the OR-HPMFSG with respect to the magnetic properties of the iron core of the rotor segments and the stator core. To calculate the temperature of the passive components using a 3-D LPTN, it is crucial to derive their losses as local heat sources. Since Ref. [19] did not provide the loss distribution for the end caps, stationary shaft, and rotating shaft, the loss distribution in the aforementioned components was determined using 3-D FEA.

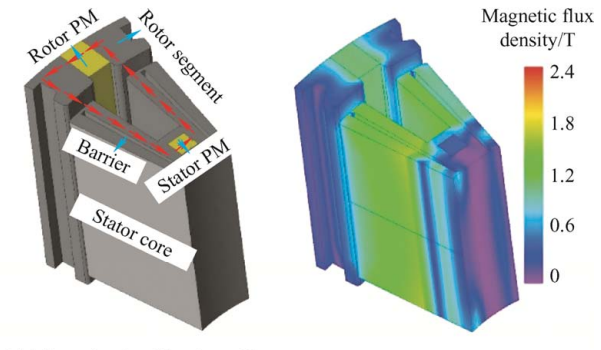

(a) Magnetization direction with main flux path (b) Flux density distribution

Fig. 2 One pole of the OR-HPMFSG

Fig. 3 presents the loss density distribution in the end caps, stationary shaft, and rotating shaft. The regions of the end caps that have been covered by the shaft and holder are responsible for the highest value of the eddy current loss density. Moreover, the areas of the stationary shaft surrounded by the stator yoke experience the maximum iron-loss density. Furthermore, the eddy current loss is the greatest when the rotating shaft is in contact with the ball bearings. Finally, Fig. 4 illustrates the losses calculated by 3-D FEA for various components of the OR-HPMFSG. In the following section, the losses are considered as heat sources in the thermal analysis, which is performed using the 3-D LPTN.

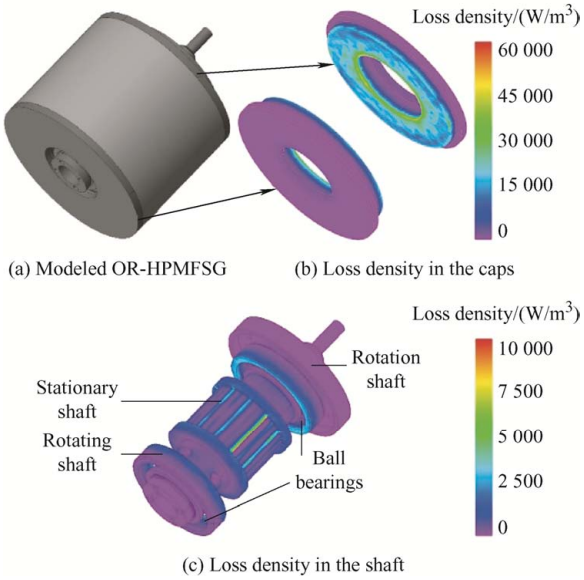

(a) Modeled OR-HPMFSG (b) Loss density in the caps

(c) Loss density in the shaft

Fig. 3 Full model and analysis of the generator

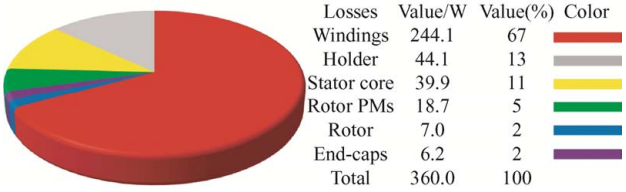

Losses	Value/W	Value(%)	Color
Windings	244.1	67	
Holder	44.1	13	
Stator core	39.9	11	
Rotor PMs	18.7	5	
Rotor	7.0	2	
End-caps	6.2	2	
Total	360.0	100	

Fig. 4 Loss distribution at the nominal conditions

3 Design of the 3-D LPTN for the OR-HPMFSG

Fig. 5 outlines the design procedure for the proposed 3-D LPTN in detail. First, the geometric dimensions serve as initial inputs. Second, the process is divided into two sections: loss calculation and thermal modeling. The losses of all active and passive components were derived using 3-D FEA. Meanwhile, to design the 3-D LPTN, boundary conditions are adopted through the identification of the heat transfer

paths, and thermal modeling is accomplished by determining the thermal resistances and capacitances of the components that are considered as thermal nodes. Finally, the temperatures of various components in both transient and steady states are derived by applying the heat equation to the thermal nodes. Notably, considering the fact that some components are subdivided into internal sections, losses for those internal sections are considered based on the loss density distribution. The thermal characteristics of the OR-HPMFSG, including the heat capacitances and thermal resistances, are analyzed, followed by the integration of the 3-D LPTN.

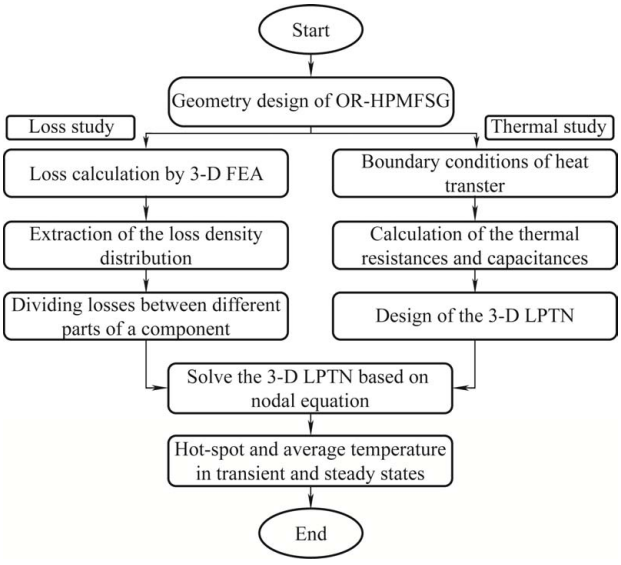

Fig. 5 Step-by-step process of thermal analysis by 3-D LPTN

3.1 Thermal characteristics

Modeling and analyzing the processes of the thermal field in a thermal network require a systematic method, which is provided by heat transfer analysis. The heat transfer process represented by the LPTN employs a network of thermal resistances and capacitances, providing an efficient and accurate analysis of the thermal behavior. In addition, each component is modeled as a thermal node, and the power losses are considered for each node as a potential heat source. The thermal storage capacity of the components is defined by the thermal capacitance, while the heat transfer rate between the thermal nodes is represented by the thermal resistance.

3.1.1 Heat capacitance

The heat capacitance must be obtained to derive the temperature changes of the components in the transient state, which are denoted as

$$C = \rho V c_p \tag{1}$$

where ρ (kg/m^3), c_p (J/kg/℃), and V denote the material density, material specific heat, and volume (m^3) of the component, respectively. Conduction, convection, and radiation are the three primary mechanisms of heat transfer, and their modeling in a thermal network is discussed in the following section.

3.1.2 Conduction

Conduction is the heat transfer process from a hotter to a cooler portion of a component owing to the difference in the temperature gradient. Thermal conduction resistance is a measure of the amount of heat that flows through a material per unit of time. Using Fourier's law, the thermal conduction resistance is calculated as follows

$$R_d = \frac{L_d}{A \times k} \tag{2}$$

where, L_d (m) represents the conduction path length, A (m^2) denotes the cross-section area of heat flow path, and k (W/m^2/℃) is the material thermal conductivity. The greater the thermal conduction resistance, the more challenging it is for thermal energy to flow across the material.

3.1.3 Convection

Convection involves heat transfer through a fluid owing to its motion and can occur naturally or be forced by a cooling system. According to Newton's law, the following equation is used to represent heat transfer via convection thermal resistance

$$R_v = \frac{1}{A \times h} \tag{3}$$

where h (W/m^2/℃) is the heat transfer coefficient, which is influenced by fluid parameters, including surface geometry and fluid properties, such as viscosity, fluid thermal conductivity, specific heat, and flow velocity. Different correlations are required for the convective coefficient calculation based on whether the flow is laminar or turbulent, and in the main flux direction.

3.1.4 Radiation

Radiation heat transfer can occur in a vacuum, in contrast to conduction and convection. The radiation thermal resistance is defined as the ratio of the

temperature difference between the two surfaces to the radiative heat transfer and is expressed as

$$R_{rad} = \frac{1}{\varepsilon_{th}\sigma_{SB}A(T_s^4 - T_a^4)(T_s - T_a)} \tag{4}$$

where ε_{th} signifies the surface emissivity, σ_{SB} is the Stefan-Boltzmann constant, T_s(℃) indicates the surface temperature, and T_a(℃) refers to the ambient temperature. The radiation resistance is nonlinear because the temperature difference increases to the fourth power level and becomes significantly more critical at high temperatures. Moreover, compared to conduction and convection, this nonlinearity makes radiation modeling more challenging and time-consuming without a noticeable improvement in accuracy. Since the OR-HPMFSG operates at low speed, the radiation effect is ignored, and conduction and convection are assumed to be the main modes of heat transfer.

3.2 Proposed 3-D LPTN

Accurate temperature estimation using the LPTN can be achieved by considering heat transfer in three dimensions: radial, axial, and circumferential. In this situation, all heat paths that flow to or dissipate from the components are examined. Conventional LPTNs assume a single node for a component and a uniform temperature distribution. However, the uniform allocation of losses leads to a concentration of heat in certain areas, which in turn causes the LPTN to exhibit inaccuracies in estimating the temperature distribution and hotspots. To investigate this critical problem, the proposed 3-D LPTN does not consider a single node for key components; instead, subnodes are provided based on the geometry and local heat to model each section of the components, such as the stator, winding, rotor segment, PM, holder, and shaft. The nodes allocated to each component of the OR-HPMFSG are shown in Fig. 6a. The thermal network contains 28 main nodes to represent the temperatures in the end-winding (EW), slot-winding (SW), left and right sides of the stator yoke (SYL and SYR), up and down sides of the stator yoke (SYU and SYD), left and right sides of the stator teeth (STL and STR), stator PM (SPM), two main rotor segments, divided into three sections ($RS_{1\text{-}1}$, $RS_{1\text{-}2}$, $RS_{1\text{-}3}$, $RS_{2\text{-}1}$, $RS_{2\text{-}2}$, $RS_{2\text{-}3}$), three section of the rotor PM ($RPM_{1,\ 2,\ 3}$), holder of segments and holder yoke (HS and HY), end cap (EC), bearing (Br), stationary and virtual shafts (SS and VS), air-gap (AG), inner air (IA), outer air (OA), and enclosed air in the left and right side of stator teeth (EAL and EAR). To represent the connections between various nodes, the contact, insulation, and convection thermal resistances are shown in Fig. 6b. To account for imperfect assembly, an equivalent interface gap is considered as the thermal contact resistance

$$R_t = \frac{L_t}{A \times k_a} \tag{5}$$

where L_t denotes the equivalent interface gap (m), and k_a is the thermal conductivity of the air or adhesive. In the 3-D LPTN, the thermal contact resistances are investigated between various regions, including the stator sections and SPM, stator sections and SS, RS and RPM, HS with RS and RPM, HY and EC, EC and VS, and Br and SS in the corresponding three dimensions. The winding insulator, which suffers from low-temperature dissipation owing to its low thermal conductivity, is also considered between the winding and stator sections. The winding insulator resistance is modeled as follows

$$R_i = \frac{L_i}{A \times k_i} \tag{6}$$

where L_i and k_i denote the insulation thickness (m) and thermal conductivity of the insulator, respectively.

Convection resistances were investigated in the internal areas of the AG, IA, EAL, and EAR and the external regions of the OA. The Taylor number was used to identify whether the AG contains laminar or turbulent flow, and subsequently, the convection resistances R_{v0} to R_{v6} were extracted. The convection coefficients in the IA, EAL, and EAR for thermal resistances R_{v7} to R_{v36} were determined by correlating the rotor speed with the fluid characteristics. Finally, through the heat transfer coefficient of the rotating and stationary components, the resistances of R_{v37} to R_{v39} offer external convection with OA.

In the following section, the thermal network for the stator side, rotor side, and passive components is presented. It is worth noting that because of the axial symmetry, only half of the components are modeled in the axial direction, and because of the symmetry in the radial-circumferential plane, only one pole of each component is modeled.

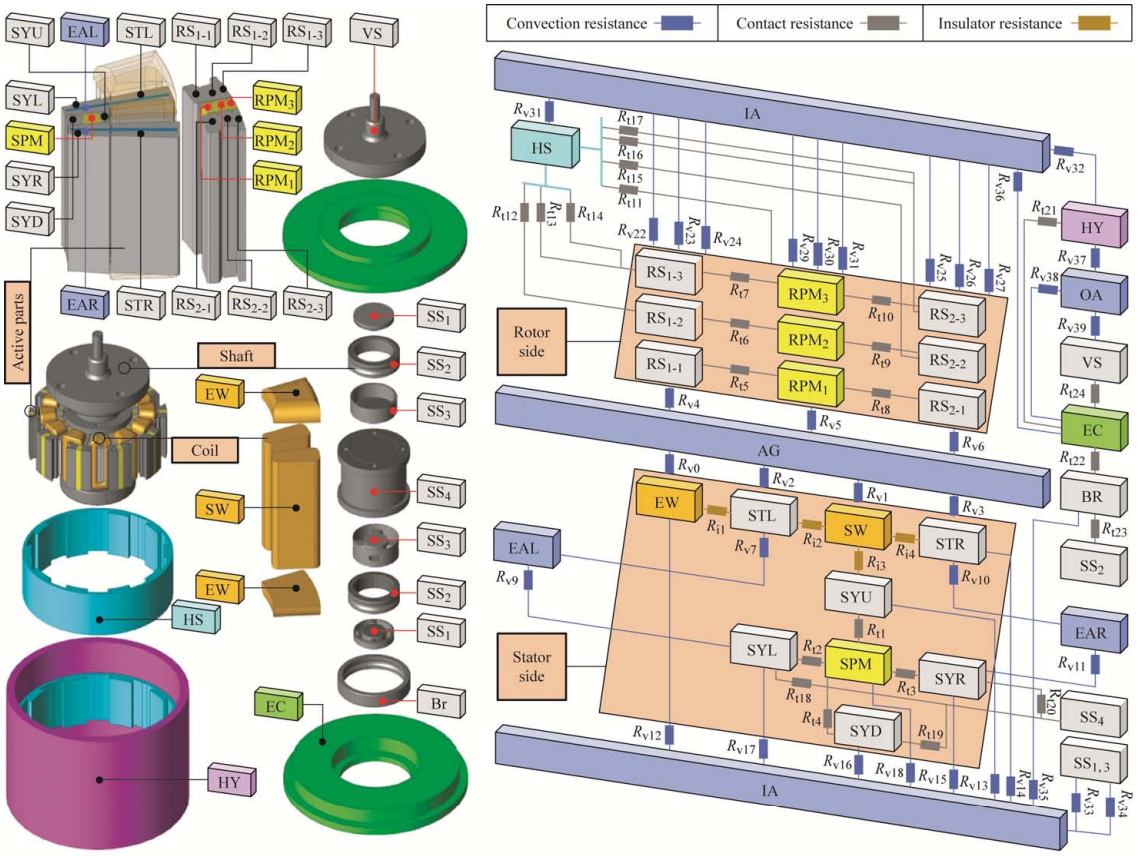

(a) Node allocation to the parts (b) Connection between nodes

Fig. 6 Schematic view of the 3-D LPTN

3.2.1 Stator core, winding, and ferrite PM

The nonuniform distribution of iron loss causes a significant temperature gradient in the stator core. In this context, this component is subdivided into six sections: SYL, SYR, SYU, SYD, STL, and STR, such that the average and hotspot temperatures could be examined precisely. As the winding is susceptible to critical temperatures owing to significant copper loss, it is necessary to split the winding into two sections, SW and EW, to increase the modeling accuracy. Fig. 7 shows the thermal circuits of the sections constituting the winding, stator core, and stator PM.

It can be observed that SYL and SYR are circumferentially connected to SYU and SYD, as well as to STL and STR via radial resistances. Except for the STL, which is connected to the EW in the axial direction as the coil is wound over the tooth, all stator sections are linked to the IA. In addition, the circumferential surfaces of the STR and STL are joined to the SW on one side, while the opposite surfaces of the STR and STL and the circumferential resistances of the SYL and SYR are related to the EAL and EAR, respectively. Moreover, the inner radial resistances of the SYD, SYL, and SYR are coupled to the SS through the corresponding contact resistances.

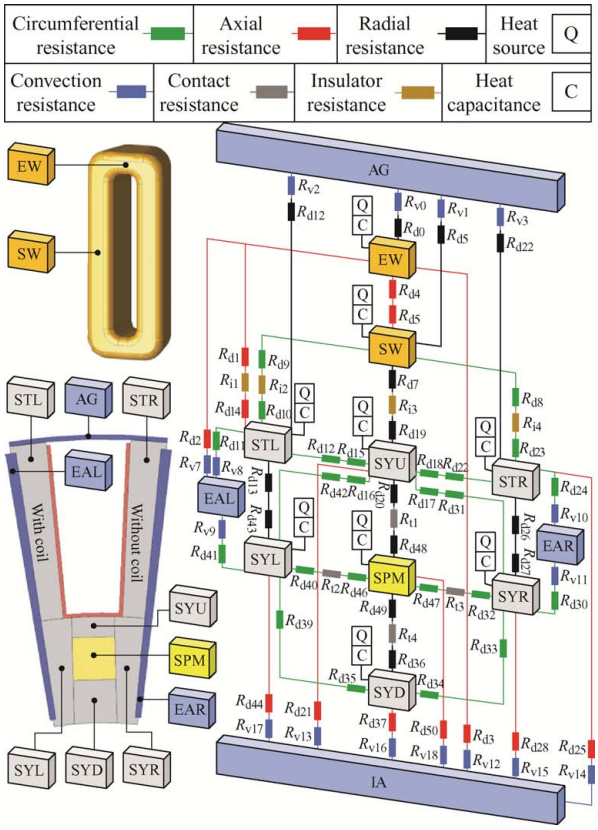

Fig. 7 Thermal nodes and circuit for one pole of the stator side

The stator core loss was assigned to the stator sections based on the average loss density extracted using 3-D FEA. In the case of the EW, the heat flows radially from the EW to the AG and axially to the SW, STL, and EAL. Importantly, owing to lamination, the thermal conductivity of the core material varies along the axial direction from that along the radial and circumferential directions.

In addition, because of the dielectric coating layer between the conductors, the thermal conductivity of the SW is anisotropic, leading to distinct conductivities in the axial and radial directions. The corresponding thermal conductivity of the SW in the axial direction can be expressed as [18]

$$k_{eq} = k_i \frac{(1+F_f)k_{co} + (1-F_f)k_i}{(1-F_f)k_{co} + (1+F_f)k_i} \tag{7}$$

where F_f is the slot-filling factor and k_{co} denotes the thermal conductivity of copper. To determine the SW and EW heat sources, the copper loss of the coil is divided by its length as follows

$$P_{SW} = \frac{P_{coil}}{(L_{SW} + L_{EW}) / L_{SW}} \tag{8}$$

$$P_{EW} = \frac{P_{coil}}{(L_{SW} + L_{EW}) / L_{EW}} \tag{9}$$

where P_{coil}, P_{SW}, and P_{EW} denote the copper losses of the coil, SW, and EW, respectively. In addition to the abovementioned parameters, L_{SW} and L_{EW} indicate the lengths of the SW and EW, respectively. Furthermore, the SPM is a cuboidal component surrounded by the stator yoke sections (SYU, SYD, SYL, and SYR). It conducts heat to SYL and SYR via R_{d46} and R_{d47} in the circumferential direction and to SYU and SYD via the radial resistances of R_{d48} and R_{d49}, respectively. Additionally, the SPM dissipates heat to the IA through an axial resistance of R_{d50} in series with a convection resistance of R_{v18}.

3.2.2 Rotor segment, NdFeB PM, and holder of segments

The outer rotor arrangement of the OR-HPMFSG dissipates considerable heat into the ambient environment. Nevertheless, it must be precisely modeled because it serves as a partition between the internal and external environments. A detailed thermal circuit for the assembly of the rotating components is shown in Fig. 8. Since the properties of RPM, which is a rare-earth PM, are strongly dependent on temperature, it is divided into three sections, RPM_1, RPM_2, and RPM_3, to improve the modeling precision. In addition, the same process is performed for the rotor segments, in which $RS_{1\text{-}1}$, $RS_{1\text{-}2}$, and $RS_{1\text{-}3}$ are the thermal nodes of one rotor segment, and $RS_{2\text{-}1}$, $RS_{2\text{-}2}$, and $RS_{2\text{-}3}$ are the sections of the second rotor segment. The holder is separated into HS and HY because HY is subjected to external convection, whereas HS is exposed to the internal fluid. According to the thermal circuit on the rotor side, all thermal nodes are exposed to IA in the axial direction. However, only $RS_{1\text{-}1}$, $RS_{2\text{-}1}$, and RPM_1 dissipate heat to AG. Radial and circumferential thermal resistances are provided to connect the HS to RPM_3, $RS_{1\text{-}2}$, $RS_{1\text{-}3}$, $RS_{2\text{-}2}$, and $RS_{2\text{-}3}$. In terms of RPM_1, heat is dissipated to the AG in the radial direction via R_{d82} in series with R_{v5} and to the IA using R_{v30} with an axial resistance of R_{d78}. In addition, heat is transferred to $RS_{2\text{-}1}$, $RS_{1\text{-}1}$, and RPM_2 through R_{d79}, R_{d80} and R_{d81}, respectively. The resistances are calculated using Eqs. (10)-(12), where k_{RPM} is the thermal conductivity of NdFeB.

$$R_{d78} = \frac{0.5L_{a,RPM_1}}{L_{r,RPM_1} L_{c,RPM_1} k_{RPM}} \tag{10}$$

$$R_{d79} = R_{d80} = \frac{0.5L_{c,RPM_1}}{0.5L_{a,RPM_1} L_{r,RPM_1} k_{RPM}} \tag{11}$$

$$R_{d81} = R_{d82} = \frac{0.5L_{r,RPM_1}}{0.5L_{a,RPM_1} L_{c,RPM_1} k_{RPM}} \tag{12}$$

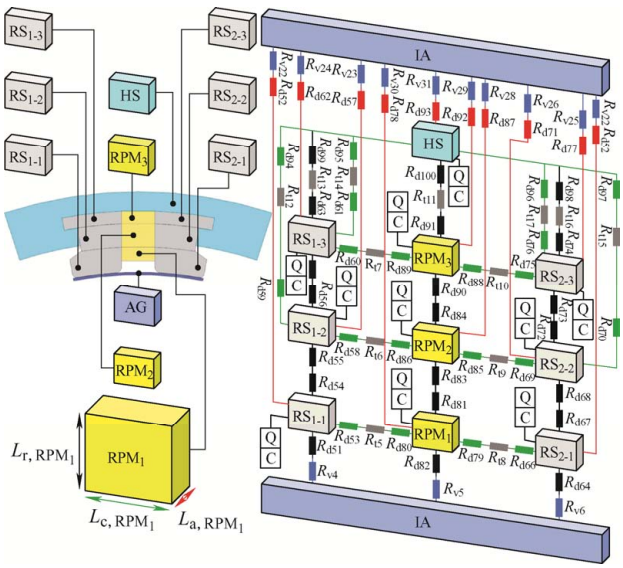

Fig. 8 Components and thermal circuit of one pole of the rotor side

3.2.3 Holder yoke, end cap, bearing, and shafts

The modeling of passive components is conventionally

ignored or is modeled in 1-D according to Ref. [22] owing to the fact that their properties are unaffected by heat and experience low temperature as a result of low power loss. However, the proposed 3-D LPTN models all the passive components, including the holder, end cap, bearing, stationary shaft, and virtual shaft, in a manner that considers the primary heat transfer paths. Fig. 9 shows the thermal circuit for the passive components, in which heat transfer in the circumferential direction is ignored. This indicates that heat is dissipated from the HY, VS, and EC to the ambient environment in the axial and radial directions. Based on the geometry, the stationary shaft is divided into four sections connected to various components and areas. Meanwhile, SS_2 is connected to Br and SS_4 is connected to the stator yoke sections in the radial direction, while SS_1 and SS_3 are subjected to IA. In addition, the bearing is connected to IA in the axial direction and to SS_2 and EC in the radial direction.

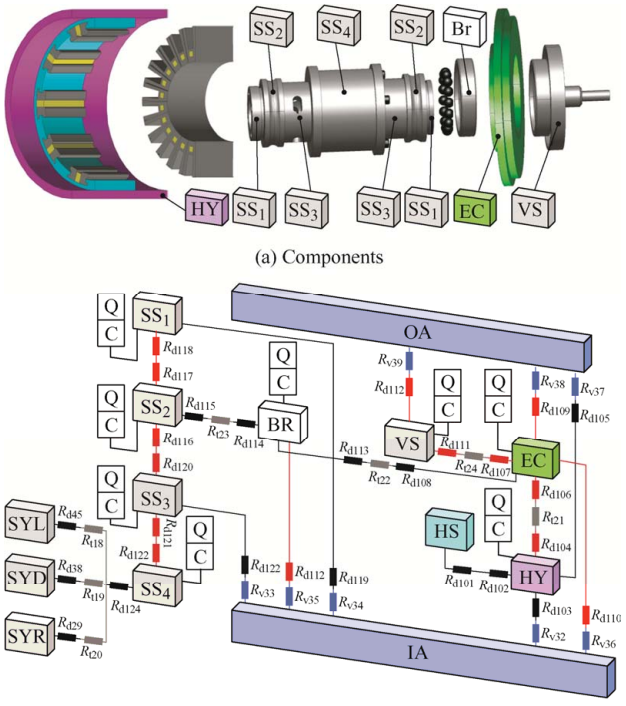

(a) Components

(b) Thermal circuit

Fig. 9 Passive components

3.3 Integrated thermal network

Following the 3-D LPTN design of the parts and the calculation of thermal resistances and capacitances, the final step is to solve the LPTN to show the transient and steady-state temperatures. The node temperature can be estimated by adjusting the heat transfer correlation in Eq. (13).

$$\sum_{m\neq 1}(T_n - T_m)G_{n,m} = C_n\frac{\mathrm{d}T_n}{\mathrm{d}t} \tag{13}$$

where T_n and T_m are the temperatures of the n^{th} and m^{th} nodes, respectively, which vary with time t, and $\boldsymbol{G}$ denotes the conductance matrix. In the following, the temperature results of the 3-D LPTN are demonstrated and verified through a comparison with 3-D FEA and an experimental test.

4 Results and discussions

Since the experimental thermal setup used to acquire the overall temperature was implemented after magnetic analysis and requires considerable time to reach a steady condition, the computational speed of alternative approaches is an important criterion. Tab. 2 presents a comparison of the proposed 3-D LPTN and 3-D FEA in terms of the respective computational times. It is evident that the proposed 3-D LPTN drastically boosts the temperature prediction speed, as the time required for both transient and steady states for 3-D FEA is 24 120 s, whereas the proposed 3-D LPTN requires only 12.43 s. Moreover, it suggests that sensitivity analyses and optimization simulations employing 3-D LPTN require significantly less time.

Tab. 2 Computation time of the proposed 3-D LPTN and 3-D FEA

Method	Steady-state/s	Transient-state/s	Total/s
3-D LPTN	4.92	7.51	12.43
3-D FEA	720	23 400	24 120

To verify the proposed 3-D LPTN, an experimental test setup of the presented 3-phase, 24/10 prototype OR-HPMFSG with 2.1 kW rated power and a nominal rotational speed of 750 r/min was developed, as shown in Fig. 10. The constructed generator was coupled to a prime mover through a transducer to acquire the input torque, the speed of which was controlled by an inverter and monitored by a tachometer. In addition, the OR-HPMFSG was connected to a 3-phase resistive load through a grounded star connection. The RMS values for the phase voltage and terminal current were recorded as 236 V and 2.9 A, respectively. Fig. 11 compares the power loss and efficiency obtained by the 3-D FEA and experimental tests. It can be noticed that the FEA results differ by 3.5% because the mechanical and AC-copper losses were ignored. The

temperature of the laboratory environment is recorded as 22.4 ℃. Three thermal sensors were placed to measure the temperatures of the stator tooth tip, end winding, and slot winding. The temperatures of the holder, endcap, and virtual shaft were monitored using a laser thermometer. It should be noted that the installation of thermal sensors for PMs was not provided because of manufacturing limitations.

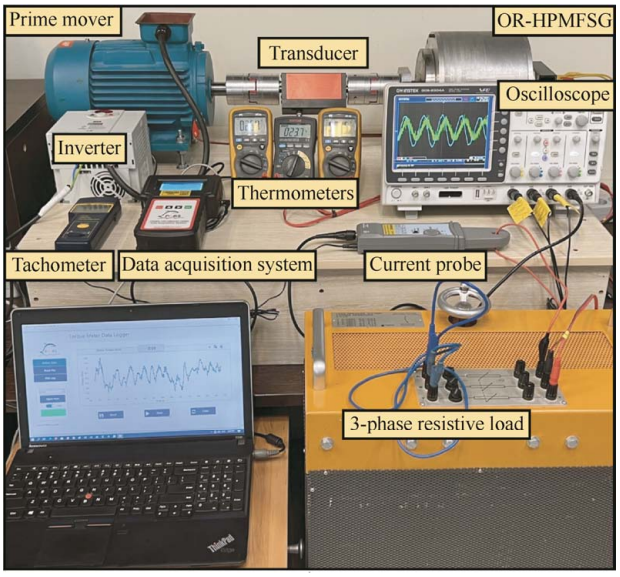

Fig. 10 Experimental test setup of the OR-HPMFSG

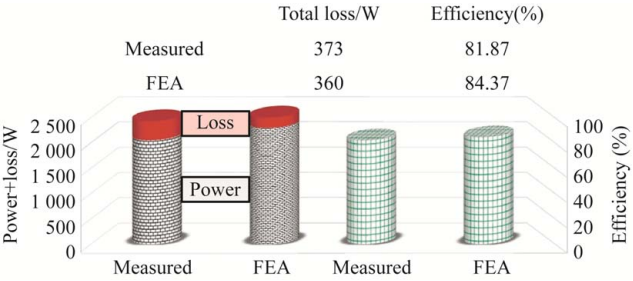

Fig. 11 Loss and efficiency estimated by FEA and experiment

When the temperature increase reaches a steady state after 150 min, the measured temperatures are reported to be under nominal operating conditions. Fig. 12 compares the transient temperature results from the proposed 3-D LPTN, 3-D FEA, and experimental tests. It is necessary to clarify that the ambient temperature for the proposed 3-D LPTN and 3-D FEA is set the same as the experimentally measured test environment temperature of 22.4 ℃. It is clear that the temperature increase trend of the 3-D LPTN is similar to that of the measured and 3-D FEA, and it also estimated the transient temperature of the components, particularly the internal components, with remarkable accuracy. Tab. 3 lists the findings of the FEA, 3-D LPTN, and experimental test, in addition to the deviation between steady-state temperatures of the 3-D LPTN and measured at the rated power/speed, 120% overspeed, and 120% overload conditions.

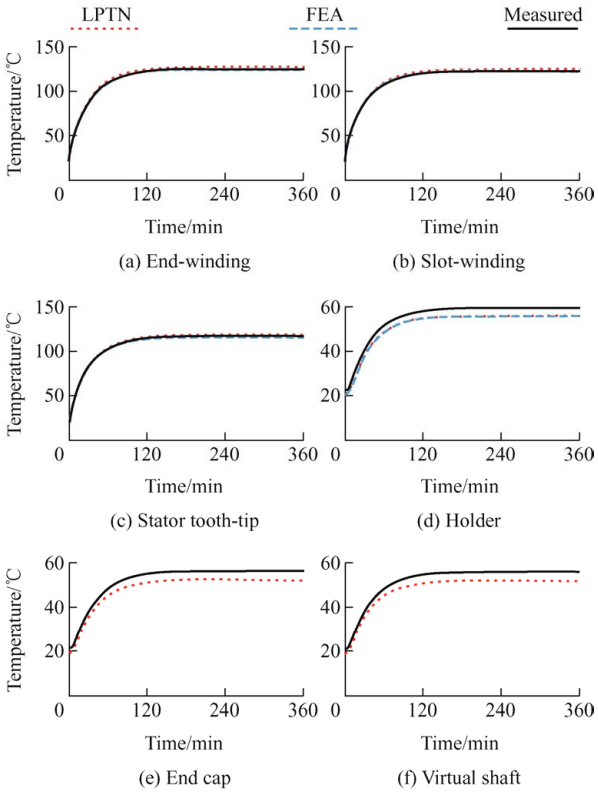

Fig. 12 Transient temperatures comparison

Tab. 3 Steady-state temperature comparison of OR-HPMFSG at different conditions

Node	FEA	3-D LPTN	Measured	Error (%)	Condition
End-winding	124	127.4	125.2	1.75	Rated
	142.4	142.2	143.75	1.5	120% load
	140.8	141.37	142.13	0.5	120% speed
Slot-winding	122.3	125.3	122.6	2.2	Rated
	141.7	139.9	142	1.49	120% load
	138.3	137.5	138.6	0.77	120% speed
Stator tooth-tip	117	119.1	117.8	1.1	Rated
	132.9	133.5	133.8	0.23	120% load
	130.8	132.76	131.8	0.73	120% speed
Holder	56.26	56.35	59.7	5.6	Rated
	63.3	64.47	67.17	4	120% load
	61.9	62.75	65.9	4.45	120% speed
End cap	55.84	52.8	56.6	6.7	Rated
	57.4	55.3	58.18	4.95	120% load
	56.2	55.65	57	2.3	120% speed
Virtual shaft	52.2	52.35	56.13	6.7	Rated
	56.7	58.2	61	4.5	120% load
	55.5	55.72	59.7	6.6	120% speed

According to the results of all three methods, the temperature distribution is as expected, with the

highest temperature in the end winding and lowest temperature in the virtual shaft. Moreover, the 3-D LPTN accurately provides the hotspot temperature, which corresponds well with the measured results, as the error between them in the rated condition is 1.75%. Additionally, the maximum deviation between the modeled and measured temperatures for the critical components of the internal areas is 2.2%, and in the external area, it is 6.7%. It should be mentioned that the maximum differences between 3-D FEA and measured temperatures are 0.93% for the hotspot and 5.7% for the external region. Moreover, the component temperature increased at overload and overspeed owing to the increasing copper and core losses, respectively. The results of the 3-D LPTN agree well with both the experimental tests and the FEA.

The temperatures at each node are listed in Tab. 4 under rated conditions. This clearly indicates that the hotspot is located in the EW. Consequently, the axial and circumferential surfaces of the STL, which are wrapped by the end windings, experienced higher temperatures. Based on the results, the proposed 3-D LPTN effectively illustrates the temperature distribution.

Tab. 4 Rated temperature of the nodes in various directions

Node position	Temperature/℃
EW_r EW_a	127.3, 127.5
SW_{ri} SW_{ro} SW_{cl} SW_{cr} SW_a	125.2, 125.2, 125.3, 125.2, 125.5
STL_{ri} STL_{ro} STL_{cl} STL_{cr} STL_a	116.8, 122, 123.2, 124.3, 124.2
SYU_{ri} SYU_{ro} SYU_{cl} SYU_{cr} SYU_a	115.5, 115.7, 115.4, 115.2, 115.5
STR_{ri} STR_{ro} STR_{cl} STR_{cr} STR_a	112.3, 117.3, 120.7, 117.9, 118.3
SYR_{ri} SYR_{ro} SYR_{cl} SYR_{cr} SYR_a	103.4, 112.3, 107, 107.2, 107.3
SYD_{ri} SYD_{ro} SYD_{cl} SYD_{cr} SYD_a	101.1, 101.7, 101.8, 101.7,101.6
SYL_{ri} SYL_{ro} SYL_{cl} SYL_{cr} SYL_a	105.5, 116.8, 113.3, 108, 111.5
SPM_{ri} SPM_{ro} SPM_{cl} SPM_{cr} SPM_a	102.7, 113.8, 107, 106.3, 107.6
$RS_{1\text{-}1,\,ri}$ $RS_{1\text{-}1,\,ro}$ $RS_{1\text{-}1,\,cl}$ $RS_{1\text{-}1,\,cr}$ $RS_{1\text{-}1,\,a}$	66.8, 64.3, 65.6, 66.6, 64.6
$RS_{1\text{-}2,\,ri}$ $RS_{1\text{-}2,\,ro}$ $RS_{1\text{-}2,\,cl}$ $RS_{1\text{-}2,\,cr}$ $RS_{1\text{-}2,\,a}$	64.3, 60.9, 60.1, 64.3, 62.6
$RS_{1\text{-}3,\,ri}$ $RS_{1\text{-}3,\,ro}$ $RS_{1\text{-}3,\,cl}$ $RS_{1\text{-}3,\,cr}$ $RS_{1\text{-}3,\,a}$	60.9, 56.7, 60, 60.4, 59.3
$RPM_{1,\,ri}$ $RPM_{1,\,ro}$ $RPM_{1,\,cl}$ $RPM_{1,\,cr}$ $PM_{1,\,a}$	67.2, 64.6, 66.78, 66.78, 64.8
$RPM_{2,\,ri}$ $RPM_{2,\,ro}$ $RPM_{2,\,cl}$ $RPM_{2,\,cr}$ $RPM_{2,\,a}$	64.6, 61.2, 64.5, 64.5, 62.7
$RPM_{3,\,ri}$ $RPM_{3,\,ro}$ $RPM_{3,\,cl}$ $RPM_{3,\,cr}$ $RPM_{3,\,a}$	61.2, 56.9 60.6, 60.6, 59.4
HS_{ri} HS_{ro} HS_{cl} HS_{cr} HS_a	54.5, 54.4, 59.8, 59.8, 56
HY_{ri} HY_{ro} HY_a	55.2, 54.3, 52.9
EC_r EC_a	53.36, 53.6
VS_r VS_a	52.3, 51.7
Br_r Br_a	66.2, 56
$SS_{1,\,r}$ $SS_{1,\,a}$ $SS_{2,\,r}$ $SS_{2,\,a}$	54.1, 52.6, 66.2, 52.6
$SS_{3,\,r}$ $SS_{3,\,a}$ $SS_{4,\,r}$ $SS_{4,\,a}$	96.3, 52.6, 99.6, 52.6
AG IA	93.6, 56

*The subscripts "r," "c," and "a" denote the radial, circumfrential, and axial directions, respectively. The subscripts "i," "o," "l," and "r" are related to the inner, outer, left, and right side surfaces, respectively.

The temperature distributions in all active and passive components of the OR-HPMFSG are shown in Fig. 13. It can be observed that a hotspot temperature of 123.1 ℃ is located in the winding, and the inner radius of the stator core is 18 ℃ cooler than the outer radius. In addition, the surfaces of the rotor PM and the rotor segments in contact with the air gap are predicted to have higher temperatures than those in other regions. The stationary shaft surfaces in direct contact with the stator yoke become more heated owing to intense stator heat flux production. Hence, the temperatures of the passive components is lower than those of the active components. Fig. 14 illustrates the temperature distribution achieved by the proposed

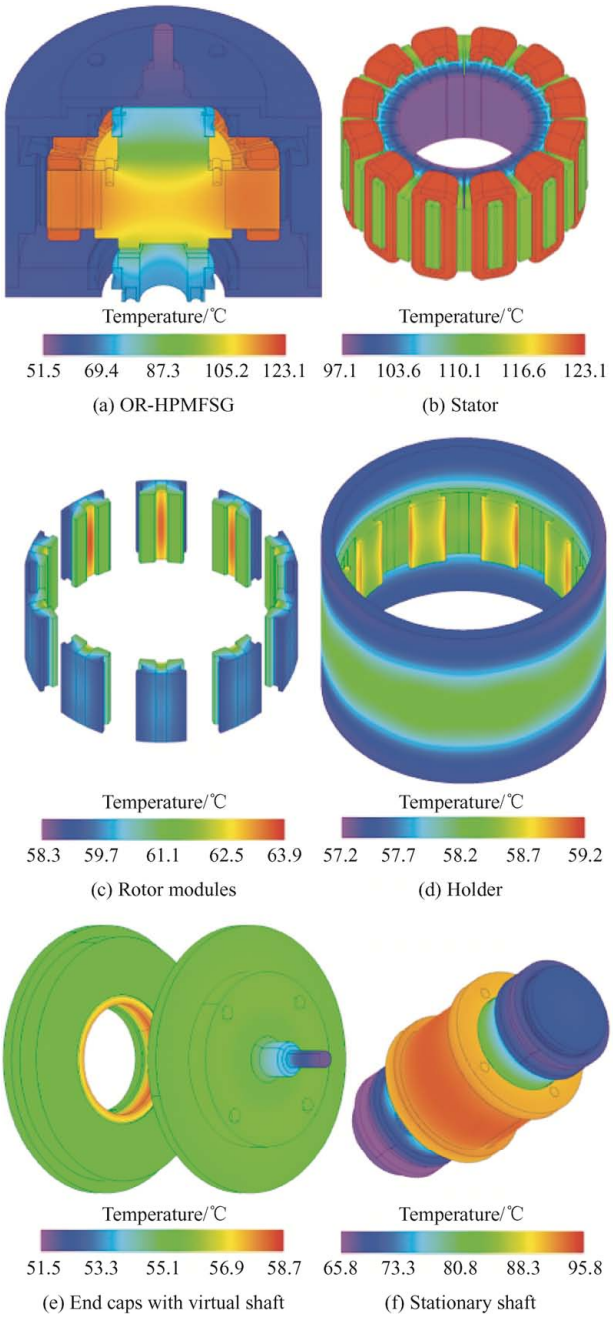

Fig. 13 Temperature distribution

3-D LPTN and the developed model of 3-D FEA in the momentous components, including the stator core, stator PM, rotor segments, rotor PM, and winding. Similar to FEA, SYD has the lowest temperature, and the wounded tooth (STL) experiences the highest temperature. Moreover, 3-D LPTN clearly demonstrates that the temperature of the wounded teeth is approximately 3.2 ℃ higher than that of the non-wounded teeth. Additionally, the error between the stator PM temperature results is less than 5%. Moreover, the rotor temperature distribution by the 3-D LPTN is identical to that of the FEA, with a higher temperature in the inner radius area.

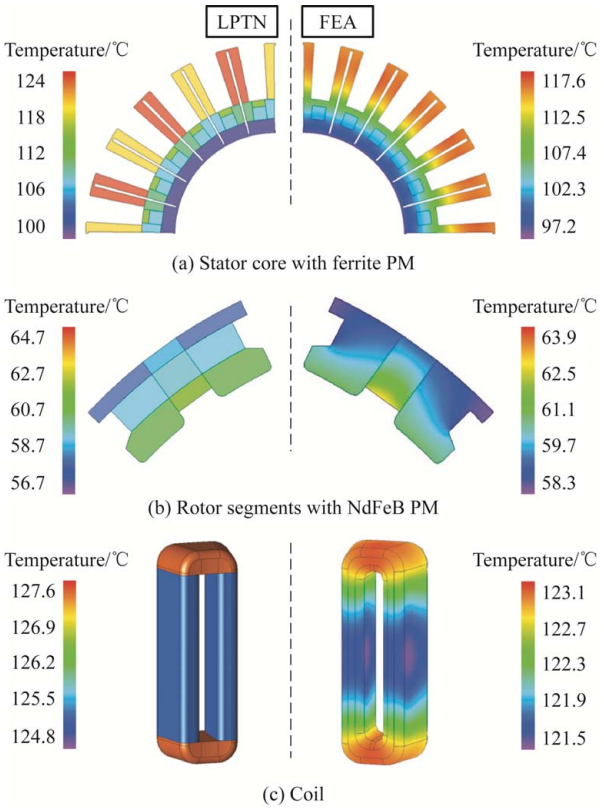

Fig. 14 Temperature distribution comparison between the proposed 3-D LPTN and FEA

Furthermore, both FEA and LPTN manifest slot-coil has aronnd 2 ℃ lower temperature than end-winding. This comparison proves that the proposed 3-D LPTN not only estimates the average temperature with acceptable accuracy but also provides a similar temperature distribution pattern.

To check the precision of the LPTN under fault conditions, in the next scenario, the proposed 3-D LPTN is employed to estimate the temperature of the components under various operating conditions.

Importantly, the comparison is reported at 175 Hz and 200% of the rated load to stimulate higher wind speeds and a larger power ratings. Notably, to prevent winding failure, the OR-HPMFSG was not subjected to an experimental test; instead, 3-D FEA, whose accuracy in thermal modeling was confirmed according to Tab. 3, is used as a valid criterion for comparison. As shown in Fig. 15a, as the rotor speed increases, an increase in temperature was observed, which can be attributed to the increased iron and PM losses. In addition, the 3-D LPTN and 3-D FEA both demonstrate that the temperature within the OR-HPMFSG increases as the load current increases because of the significant heat released from copper loss. In these scenarios, 3-D LPTN results are perfectly consistent with 3-D FEA, as the error for the winding, which is the most vulnerable component to the temperature, is less than 3%. Furthermore, the 3-D LPTN proves that the rotor PM experiences a lower temperature than the stator PM, which ensures safe operation against demagnetization. Overall, the proposed 3-D LPTN can be generalized to high-power OR-HPMFSGs and can be used for optimizing designs to improve thermal performance with high accuracy and less time.

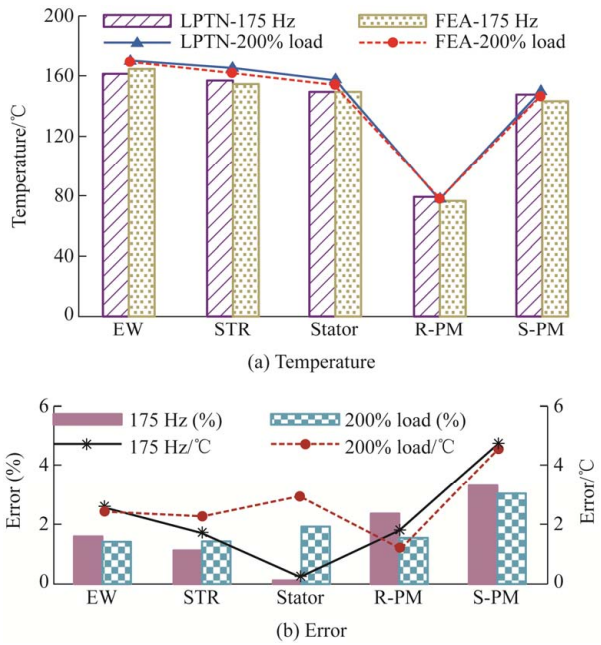

Fig. 15 Temperature rise analysis in various operating ranges by the 3-D LPTN and FEA

5 Conclusions

In this study, a 3-D LPTN was designed for the OR-HPMFSG, which employs different types of PMs in the stator and rotor. To achieve hotspot and average temperatures, the 3-D LPTN divided the generator into several discrete thermal nodes based on the geometry of the components and heat transfer paths identified and modeled in various internal and external regions. The problem of low computational speed of the 3-D FEA was solved using the proposed 3-D LPTN, making it 1 940 times faster. Through experimental testing under nominal conditions, the accuracy of the 3-D LPTN was validated in both transient and steady states, as the maximum error for the hot-spot was 1.75%. Moreover, the 3-D LPTN is a potential candidate for estimating the temperature of all active and passive components. In contrast to typical LPTNs, the proposed 3-D LPTN is a powerful alternative to FEA, primarily because the temperature distributions in the stator core and winding are achieved with remarkable accuracy. The 3-D LPTN was assessed in various operating ranges, and the results were consistent with the 3-D FEA, whose maximum deviation for vulnerable components was approximately 5%. Therefore, the proposed 3-D LPTN can be considered comprehensive, fast, and accurate for the temperature distribution analysis of the OR-HPFSMG. Moreover, it can be employed at various power-speed ranges and generalized to high-power scales. Furthermore, by adopting two types of PMs and transferring the rare-earth PM to the rotor and ferrite PM to the stator, it was shown that there is no risk of PM demagnetization in the OR-HPMFSG when using the proposed 3-D LPTN.

References

[1] W Ullah, F Khan, S Hussain, et al. A novel dual port dual rotor wound field flux switching generator with uniform and non-uniform rotor poles for counter-rotating wind power generation. *IEEE Transactions on Energy Conversion*, 2023, 38(4): 2420-2433.

[2] M Salehi, A Darabi, A Ghaheri, et al. Design and analysis of concentrated field TFPM generator for direct-drive wind turbines. *2021 29th Iranian Conference on Electrical Engineering (ICEE)*, May 18-20, 2021, Tehran, Iran. IEEE, 2021: 335-339.

[3] S A Mirnikjoo, K Abbaszadeh, S E Abdollahi. Multiobjective design optimization of a double-sided flux switching permanent magnet generator for counter-rotating wind turbine applications. *IEEE Transactions on Industrial Electronics*, 2020, 68(8): 6640-6649.

[4] Z Wu, Z Q Zhu, S Cai, et al. Enhancement of torque density in wound field switched flux machines with partitioned stators using assisted ferrites. *Chinese Journal of Electrical Engineering*, 2021, 7(3): 42-51.

[5] V Madonna, A Walker, P Giangrande, et al. Improved thermal management and analysis for stator end-windings of electrical machines. *IEEE Transactions on Industrial Electronics*, 2018, 66(7): 5057-5069.

[6] A Almounajjed, A K Sahoo, M K Kumar, et al. Stator fault diagnosis of induction motor based on discrete wavelet analysis and neural network technique. *Chinese Journal of Electrical Engineering*, 2023, 9(1): 142-157.

[7] W Zhang, Y Xu, Y Huang, et al. Reduction of high-frequency vibration noise for dual-branch three-phase permanent magnet synchronous motors. *Chinese Journal of Electrical Engineering*, 2020, 6(2): 42-51.

[8] A Zarghani, S M Saghin, A Ghaheri, et al. Magneto-thermal analysis of a novel excited outer rotor flux-switching PM machine. *2023 14th Power Electronics, Drive Systems, and Technologies Conference (PEDSTC)*, January 31-February 2, 2023, Babol, Iran. IEEE, 2023: 1-6.

[9] L Yan, Z Dong, S Zhang. Thermal analysis of a novel linear oscillating machine based on direct oil-cooling windings. *IEEE Transactions on Energy Conversion*, 2021, 37(2): 1042-1051.

[10] X Zhang, P Fu, Y Ma, et al. No-load iron loss model for a fractional-slot surface-mounted permanent magnet motor based on magnetic field analytical calculation. *Chinese Journal of Electrical Engineering*, 2018, 4(4): 71-79.

[11] D Liang, Z Zhu, J Feng, et al. Estimation of 3-D magnet temperature distribution based on lumped-parameter and analytical hybrid thermal model for SPMSM. *IEEE Transactions on Energy Conversion*, 2021, 37(1): 515-525.

[12] Q Chen, Y Fan, J Chen, et al. A new analytical thermal model of distributed winding wheel machine for electric vehicles. *IEEE Transactions on Vehicular Technology*, 2022, 71(12): 12691-12700.

[13] G Li, J Ojeda, E Hoang, et al. Thermal-electromagnetic analysis for driving cycles of embedded flux-switching permanent-magnet motors. *IEEE Transactions on Vehicular Technology*, 2011, 61(1): 140-151.

[14] G Li, J Ojeda, E Hoang, et al. Thermal-electromagnetic analysis of a fault-tolerant dual-star flux-switching permanent magnet motor for critical applications. *IET Electric Power Applications*, 2011, 5(6): 503-513.

[15] X Cai, M Cheng, S Zhu, et al. Thermal modeling of flux-switching permanent-magnet machines considering anisotropic conductivity and thermal contact resistance. *IEEE Transactions on Industrial Electronics*, 2016, 63(6): 3355-3365.

[16] L Mo, X Zhu, T Zhang, et al. Temperature rise calculation of a flux-switching permanent-magnet double-rotor machine using electromagnetic-thermal coupling analysis. *IEEE Transactions on Magnetics*, 2017, 54(3): 1-4.

[17] L Mo, T Zhang, Q Lu. Thermal analysis of a flux-switching permanent-magnet double-rotor machine with a 3-D thermal network model. *IEEE Transactions on Applied Superconductivity*, 2019, 29(2): 1-5.

[18] A Zarghani, H Torkaman, N Arbab, et al. Lumped parameter thermal network for thermal analysis of a rotor-excited axial flux switching machine with electromagnetic-thermal design. *Measurement*, 2022, 193: 110971.

[19] M Farahzadi, K Abbaszadeh, S Mirnikjoo. Electromagnetic-thermal analysis of a hybrid-excited flux switching permanent magnet generator for wind turbine application. *IEEE Transactions on Energy Conversion*, 2023, 38(3): 1962-1973.

Ali Zarghani was born in Mashhad, Iran, in 1997. He received a B.S. degree from the University of Birjand, Birjand, Iran, in 2018 and a M.S. degree from Shahid Beheshti University, Tehran, Iran, in 2021, both in Power Electrical Engineering. Since 2021, he has been a Research Assistant in the Faculty of Electrical Engineering at Shahid Beheshti University, Tehran, Iran. His research interests include analytical and finite element method development for multi-physics (electromagnetic, thermal, and mechanical) design, modeling, analysis, optimization, and manufacturing of various electromagnetic devices, with a focus on radial and axial flux PM machines for transportation and renewable energy applications.

Mohammad Farahzadi was born in Tehran, Iran. He received his M.S. degree in Power Electronics and Electric Machines in 2021. He is an Electrical Machine Designer at the Niroo Research Institute and a Researcher in the Laboratory of the K. N. Toosi University of Technology in Tehran, Iran. His research interests include mechanical and electromagnetic analyses by FEM (2D/3D), assessment of demagnetization of permanent magnets, thermal modeling by FEM, LPM, and CFD, as well as design, optimization, and prototyping of electric machines, especially machines of the flux switching permanent magnet, permanent magnet assisted synchronous reluctance, radial flux permanent magnet, axial flux permanent magnet, and doubly salient permanent magnet.

Aghil Ghaheri received the B.Sc. degree in Electrical Engineering from Shahrood University of Technology, Shahrood, Iran, in 2014, and the M.Sc. and Ph.D. degrees in Electrical Engineering from Shahid Beheshti University, Tehran, Iran, in 2016 and 2022, respectively, where he is currently working as a Postdoctoral Researcher at the Power Electronics and Motor Drives Laboratory. His research interests include permanent magnet and switched-reluctance machines, magnetic gears, and wireless power transfer systems. He has a strong focus on BLDC, flux switching, transverse flux, axial field PM synchronous, flux modulated machines, coaxial magnetic gears, and PCB motors for renewable energy, automotive and household applications. His expertise is finite element analysis, analytical modelling, optimization, manufacturing, and test of electrical machines.

Karim Abbaszadeh (Senior Member, IEEE) received the B.S. degree in Communication Engineering from the Khajeh Nasir Toosi University of Technology, Tehran, Iran, in 1991, and the M.S. and Ph.D. degrees in Electrical Engineering from the Amir Kabir University of Technology, Tehran, Iran, in 1997 and 2000, respectively. From 2001 to 2003, he was a Research Assistant with the Department of Electrical Engineering, Texas A&M University, College Station, TX, USA. He is currently a Professor with the Department of Electrical Engineering, Khajeh Nasir Toosi University of Technology, Tehran, Iran. He is actively involved in presenting short courses and consulting in his area of expertise to various industries. He is the author of more than 50 published journal articles. His research interests include power electronic and DC-DC and DC-AC converters, electric machinery, variable-speed drives, and propulsion applications.